



Numerical investigation of the water entry of inclined cylinders using dynamic sliding mesh method

Fan Chen, Wenjie Zhong, Decheng Wan*

Computational Marine Hydrodynamic Lab (CMHL), School of Naval Architecture, Ocean and Civil Engineering, Shanghai Jiao Tong University, Shanghai, 200240, China

ARTICLE INFO

Keywords:

Water entry
Dynamic mesh handling
OpenFOAM
Multiphase flow
Dimensional analysis
3D simulation

ABSTRACT

There is a lack of considerations on water entry problems of inclined cylinders with the same mass, which is important to practical engineering problems such as hydrodynamic performance optimization. Therefore, this work focuses on the effects of diameter-length ratio and water entry angles on the hydrodynamic forces on cylinders with the same mass. A numerical model for the water entry of inclined cylinders is developed. A novel dynamic sliding mesh method is implemented in OpenFOAM based on the coupling of the sliding mesh and mesh morphing methods. A spring-like mesh motion strategy is proposed. The major advantages of this self-implemented mesh handling method are on accommodation of the large amplitude of the six degree-of-freedom motion of a cylinder (rigid body) and the preservation of the mesh non-orthogonality. By comparing with a laboratory study and another numerical simulation, the proposed numerical model shows a good consistency. The effects of the aforementioned parameters on the pressure forces and cylinders' motions are investigated. A dimensional analysis is conducted to find the correlation between the maximum vertical pressure force and various parameters. An equation is proposed with a good agreement with the numerical results, which can provide references for practical water entry problems. The developed model can also be used in the simulations of more complicated water entry scenarios and ship hull slamming.

1. Introduction

Water entry of objects is a common physical process in coastal and ocean engineering, e.g. the release of lifeboats (Ma et al., 2018), landing of seaplanes (Barjasteh et al., 2016) and the recovery of spacecrafts (Seddon and Moatamedi, 2006). The research of water entry problems plays an essential role in structure designs and trajectory predictions (Yan et al., 2009; Xia et al., 2020). However, water entry problems involve complex physical phenomena, such as the violent fluid-structure interaction (Cooke and Peregrine, 1995) and complicated air cavity dynamics (Sun et al., 2021). Water entry problems still have not been fully understood since some pioneer works were conducted at the early stage (e.g. Worthington and Cole, 1897; von Karman, 1929; Wagner, 1932).

Water entry of a cylinder always attracts attentions from a large number of researchers and engineers, as this simple geometry can provide reference for structures such as the projectile and the underwater vehicle in practical engineering problems. For horizontal and vertical cylinders impacting into water, there have been a number of studies, e.g.

Greenhow and Lin (1983), Sun and Faltinsen (2006), Zhu et al. (2007), Sun et al. (2018) and Xiang et al. (2020). In recent years, the water entry of inclined cylinders gradually gains increasing considerations, due to its unique characteristics in hydrodynamics such as the asymmetric pressure distribution and cavity evolution as highlighted in Wei and Hu (2015) and Sun et al. (2021).

One research focus on the water entry of inclined cylinders is on the resultant flow field. Wei and Shi (2012) first experimentally investigated the cavitation shape during the water entry of inclined cylinders. The evolution of cavity during water entry was further studied in Wei and Hu (2014, 2015). Hou et al. (2018) applied both numerical and experimental methods to simulate the water entry of an inclined cylinder. The focus was on the cavity evolution under the conditions of different water entry angles. Liu et al. (2020) numerically examined the evolution of vortex characteristics when the inclined cylinder impacts into water at a constant initial water entry angle, where a secondary closure process was identified in the high-speed water entry process. Another research focus of the water entry of inclined cylinders is on the hydrodynamic force and cylinders' motions. Wei and Hu (2015) calculated the drag and

* Corresponding author.

E-mail address: dcwan@sjtu.edu.cn (D. Wan).

lift forces based on the measured accelerations. The effect of the water entry angle on these forces' coefficients were investigated. [Iranmanesh and Passandideh-Fard \(2017\)](#) conducted a series of numerical simulations to investigate the effect of different parameters (i.e. the cylinder diameter, length, density and the water entry velocity) on a cylinder's penetration depth after impacting into the water body. [Nguyen et al. \(2021\)](#) proposed a new numerical model by adopting the Tait equation of state as the governing equation. This model was then used to study the effect of the impact velocity and cylinder density on the cylinder's motion.

However, although the parameters, such as the water entry angle and cylinder length and diameter, were considered in the above studies, these parameters were varied independently. It appears that no studies have focused on the effects of the aforementioned parameters on the hydrodynamic forces and motions of cylinders with the same mass. However, in some practical engineering applications such as the optimization of the structure's hydrodynamic performance, the mass of object is already given or limited to a certain value as illustrated in [Liang et al. \(2016\)](#), [Rodríguez et al. \(2020\)](#) and [Zhang et al. \(2020\)](#). To address the lack of considerations on the parameters' effect on cylinders with the same mass, numerical simulation is a relatively suitable approach, given that theoretical analysis has still been limited in simplified and idealised water entry problems; and laboratory tests may require large expenses to simulate the water entry of cylinders with various parameters.

Based on current numerical methods capable of simulating water entry problems with a large motion amplitude of the falling cylinder, the commonly used methods include the overset grid method (OGM), smooth particle hydrodynamics (SPH) and mesh morphing method. Given that OGM requires certain overlapping areas between different meshes, it increases the complicity in creating meshes. Moreover, it requires some computational resources to recognise and evaluate the boundary of the solid body. SPH is computationally expensive when simulating three-dimensional problems. The mesh morphing method, in contrast, possesses relative advantages on mesh generation and computational expense. It is usually coupled with the sliding mesh approach, as demonstrated in e.g. [Jasak \(2009\)](#) and [Liu et al. \(2017\)](#), in order to simulate six degree-of-freedom (DoF) motion of the object. However, this approach can only accommodate relatively small motion amplitude, as the large displacement can still lead to largely deformed mesh cells, resulting in computation divergence. Although some topological change methods can solve this problem, the efficient algorithm for general topological changing situations is still lacking.

In this work, a novel dynamic sliding mesh method is proposed and implemented within the framework of the widely used open source computational fluid dynamic code OpenFOAM. A numerical model will be set up to simulate the water entry of inclined cylinders. This paper is structured as follows. Details of the numerical model are given in Section 2, including the governing equations, the newly implemented mesh handling method as well as the numerical setup. Section 3 provides the results of the numerical simulations and the relevant discussion, which is followed by the conclusions drawn in Section 4.

2. Numerical model

The modelling of water entry of an inclined cylinder is developed based on the multiphase flow solver *interFoam* and a self-implemented dynamic mesh handling class *sixDoFAMI* in OpenFOAM version 7. The cylinder is assumed to be a rigid body in this work. The governing equations for the multiphase flow will be given in this section, which is followed by the description of the novel dynamic mesh method and the numerical setup.

2.1. Governing equations

The water entry process involves violent two-phase flow, requiring the turbulence model and the interface tracking method. In this

numerical modelling, the two-phase (water and air) flow is assumed to be incompressible and immiscible. For tracking the interface between the two phases, the Volume of Fluid method is adopted. In this method, the phase fraction is introduced to denote the water volume accounted for a cell. In order to capture the turbulent flow characteristics, the Reynolds Averaged Navier-Stokes (RANS) equations with the Shear Stress Transportation (SST) $k - \omega$ model as the closure are solved. This SST $k - \omega$ model possesses advantages on the simulation of both free surface and boundary flows ([Nguyen et al., 2020](#)). It has been applied in a number of numerical simulations of water entry problems, as demonstrated in e.g. [Liu et al. \(2020\)](#), [Moradi et al. \(2021\)](#) and [Sun et al. \(2021\)](#).

The governing equations for the multiphase flow are thus given as:

$$\frac{\partial \bar{u}_i}{\partial x_i} = 0, \quad (1)$$

$$\frac{\partial(\rho \bar{u}_i)}{\partial t} + \frac{\partial(\rho \bar{u}_i \bar{u}_j)}{\partial x_j} = -\frac{\partial p}{\partial x_i} + \frac{\partial}{\partial x_j} \left[\mu_{eff} \left(\frac{\partial \bar{u}_i}{\partial x_j} + \frac{\partial \bar{u}_j}{\partial x_i} \right) - \rho \bar{u}_i \bar{u}_j' \right] + \rho g_i + f_i, \quad (2)$$

$$\frac{\partial \alpha}{\partial t} + \frac{\partial \bar{u}_i \alpha}{\partial x_i} + \frac{\partial}{\partial x_i} \left[c |\bar{u}_i| \frac{\partial \alpha}{\partial x_i} \right] / \left| \frac{\partial \alpha}{\partial x_i} \right| \alpha (1 - \alpha) = 0. \quad (3)$$

In Eqs. (1) and (2), $\bar{\cdot}$ is the averaged operator, u_i ($i = 1, 2, 3$) the fluid velocity consisting of the mean \bar{u}_i and the fluctuating fluid velocity u_i' , x_i the coordinate component in each direction, ρ the fluid density and p denotes the fluid pressure. The effective dynamic viscosity μ_{eff} is the sum of the turbulent μ_t and fluid dynamic viscosity μ . The variable g_i denotes the gravitational acceleration and $f_i = \sigma_s \kappa \partial \alpha / \partial x_i$ is the surface tension force where σ_s is the surface tension coefficient, κ the curvature at the interface and α ($0 \leq \alpha \leq 1$) is the phase fraction. Equation (3) is a transport equation for updating the interface at each time step. The third term on the left-hand side of Eq. (3) is an artificial compression term added to obtain a sharp interface between the two phases, where c denotes the interface compression coefficient. Note that for the air-water interface, ρ and μ should be evaluated using α by $\rho = \alpha \rho_w + (1 - \alpha) \rho_a$ and $\mu = \alpha \mu_w + (1 - \alpha) \mu_a$, respectively. The term $\rho \bar{u}_i \bar{u}_j'$ in Eq. (2) is Reynolds stress tensor and it is obtained based on Boussinesq's hypothesis

$$\rho \bar{u}_i \bar{u}_j' = -\mu_t \left(\frac{\partial \bar{u}_i}{\partial x_j} + \frac{\partial \bar{u}_j}{\partial x_i} \right) + \frac{2}{3} k \delta_{ij}, \quad (4)$$

where δ_{ij} is Kronecker delta function, μ_t and the turbulent kinetic k are calculated by the following equations:

$$\mu_t = \rho \frac{k}{\omega}, \quad (5)$$

$$\frac{\partial(\rho k)}{\partial t} + \frac{\partial(\rho k \bar{u}_i)}{\partial x_i} = \mu_t \frac{\partial \bar{u}_i}{\partial x_j} \left(\frac{\partial \bar{u}_i}{\partial x_j} + \frac{\partial \bar{u}_j}{\partial x_i} \right) + \frac{\partial}{\partial x_i} \left[(\mu + \sigma_k \mu_t) \frac{\partial k}{\partial x_i} \right] - \rho \beta^* k \omega, \quad (6)$$

$$\begin{aligned} \frac{\partial(\rho \omega)}{\partial t} + \frac{\partial(\rho \omega \bar{u}_i)}{\partial x_i} &= \frac{\partial}{\partial x_i} \left[(\mu + \sigma_\omega \mu_t) \frac{\partial \omega}{\partial x_i} \right] + \gamma \mu_t \frac{\partial \bar{u}_i}{\partial x_j} \left(\frac{\partial \bar{u}_i}{\partial x_j} + \frac{\partial \bar{u}_j}{\partial x_i} \right) - \rho \beta f_\rho \omega^2 \\ &+ 2\rho(1 - F_1) \sigma_{\omega 2} \frac{1}{\omega} \frac{\partial k}{\partial x_i} \frac{\partial \omega}{\partial x_i}. \end{aligned} \quad (7)$$

In Eqs. (5) to (7), $k = 3(u'_i I)^2 / 2$ with $I = 0.05$ denoting the turbulent intensity, $\omega = k^{0.5} / l$ turbulent dissipation rate, $\beta^* = 0.09$ and $\sigma_{\omega 2} = 0.856$ are the constants. The variable F_1 denotes a blending function used to calculate the remaining constants σ_k , σ_ω and γ ([Menter et al., 2003](#)).

2.2. Dynamic mesh handling method

In order to accommodate the large amplitude of the six DoF motion of the falling cylinder impacting into water, a dynamic sliding mesh

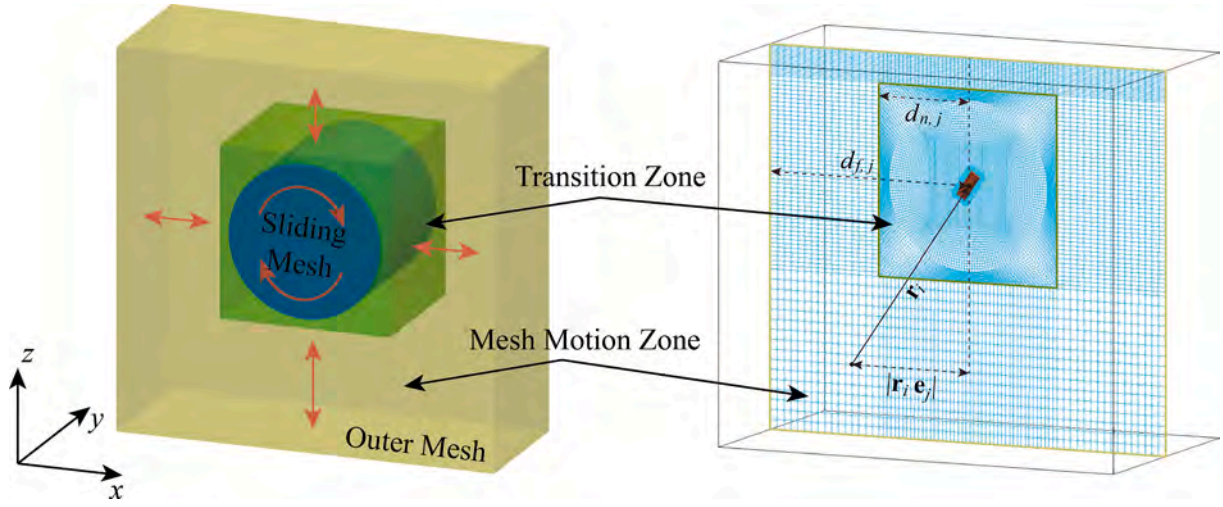


Fig. 1. Illustration of the computational domain consisted of the sliding mesh and the outer mesh.

handling method has been implemented. For the achievement of the translation and rotation of the moving cylinder, the computational domain is divided into two different meshes (Fig. 1), namely the sliding and outer meshes. The body-fitted sliding mesh contains the moving cylinder. The grid points move with the falling cylinder and perform both translation and rotation, i.e. the mesh points have no motion relative to the cylinder. Moreover, the centre of the sliding mesh remains the same location as the centre of rotation (CoR) of the cylinder during the mesh movement. Note that the cylinder's CoR is the same as its centre of mass (CoM) in the numerical simulation. Therefore, for points within the sliding mesh, each point's displacement $\Delta \mathbf{x}_i = (\Delta x_{i,1}, \Delta x_{i,2}, \Delta x_{i,3})$ is

$$\Delta \mathbf{x}_i = \Delta \mathbf{x}_c + \mathbf{r}_i \times \boldsymbol{\omega}, \quad (8)$$

where $\Delta \mathbf{x}_c = \mathbf{x}_c - \mathbf{x}_{c0}$ is the displacement of the CoM of the sliding mesh, with \mathbf{x}_c and \mathbf{x}_{c0} being the location vector of CoM at the current and initial moments in time, respectively. The vector \mathbf{r}_i points from each grid point to the CoM and $\boldsymbol{\omega}$ denotes the angular velocity vector of the cylinder (Fig. 1). In this work, \mathbf{x}_c and $\boldsymbol{\omega}$ are obtained by the introduced six DoF motion solver in *sixDoFAMI*.

The outer mesh is the remaining area of the computational domain. It only undergoes the mesh morphing depending on the location of the sliding mesh. For accommodating the large displacement of falling cylinders in the computational domain, a spring-like mesh motion strategy is proposed. The outer mesh is divided into two zones, namely the transition and mesh motion zones, as shown in Fig. 1. Each zone has its own mesh movement strategy. For points in the translation zone within the outer mesh, $\Delta \mathbf{x}_i = \Delta \mathbf{x}_c$. For points in the mesh motion zone, $\Delta \mathbf{x}_i$ is obtained by

$$\Delta x_{i,j} = \frac{d_{f,j} - \max(|\mathbf{r}_i \mathbf{e}_j|, d_{n,j})}{d_{f,j} - d_{n,j}} \Delta x_{c,j}. \quad (9)$$

In Eq. (9), the subscript j ($j = 1, 2, 3$) denotes the component of vectors along each axis. The variables $d_{f,j}$ and $d_{n,j}$ are the distances between the cylinder's CoM to the closer outer boundary of the entire computational domain and to the closer transition zone boundary, respectively, along each axis (as shown in Fig. 1). The unit vector along each axis is expressed as \mathbf{e}_j . By using this spring-like mesh motion strategy, the topologies of the sliding and outer meshes remain identical as the cylinder moves in the domain, respectively. The allowed motion amplitude of the cylinder is significantly increased. Compared with the commonly used approach that solves the Laplace equation to move the grid points, this mesh motion strategy is relatively simple and efficient. Additionally, the non-orthogonality of the mesh does not change in each mesh such that the numerical errors caused by this can be avoided.

The communication of the field data between the sliding and outer meshes is achieved by the sliding interface technique proposed by Beaudoin and Jasak (2008). Fig. 2 shows the main concepts in this method. The face area weighted method is utilised to evaluate the cells from one side to the other. Here, as a simple example, the evaluation of the variable φ_i in cell i in the outer mesh (Fig. 2) is given as below:

$$\varphi_i = \sum_k w_{jk} \varphi_{jk} = w_{j0} \varphi_j + w_{j1} \varphi_{j+1}, \quad (10)$$

where k denotes the number of the cells within the sliding mesh that intersects with the cell i , the weightings w_{jk} ($0 < w_{jk} < 1$) are the fractions of each intersected face' area accounted for the bottom face area of

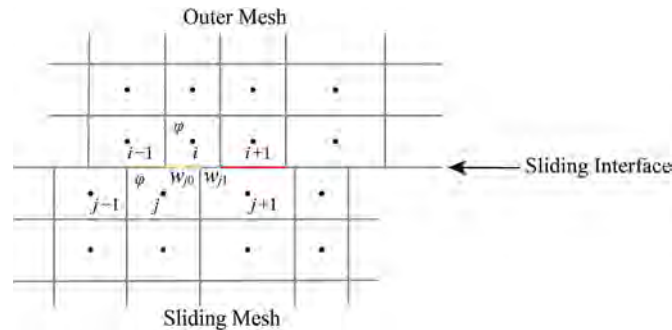


Fig. 2. Illustration of the main concepts in the sliding interface approach.

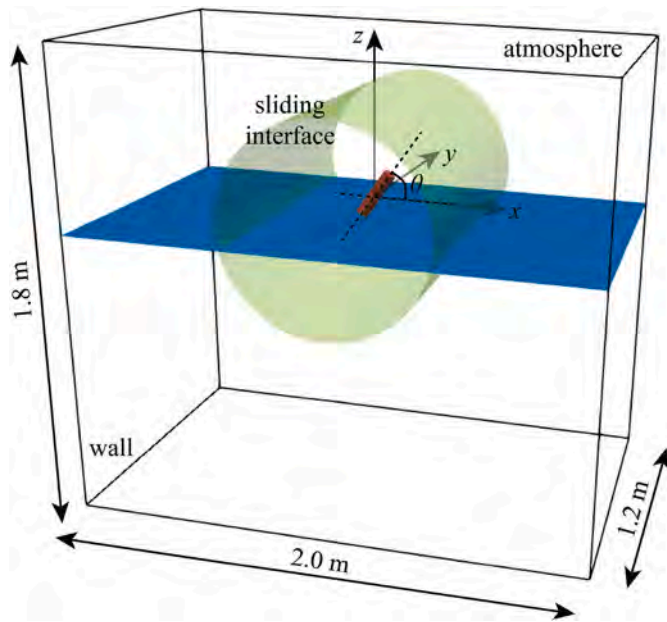


Fig. 3. Sketch of the computational domain.

cell i .

2.3. Numerical setup

A Cartesian coordinate as shown in Fig. 3 is established to describe the computational domain for simulating the water entry of inclined cylinders. The origin is located at the CoR of the cylinder, with the z -axis pointing vertically upwards and the directions of the x - and y -axes following the right-hand rule. The entire domain is symmetric about the xz and yz planes (Fig. 3). The determinations of the computational domain and the cylinder dimensions are referred to some laboratory tests (Wei and Hu, 2014; 2015) and numerical simulations (Liu et al., 2020; Sun et al., 2020). The length, width and height of the domain are 2.0 m, 1.2 m and 1.8 m, respectively. The water entry angle of the cylinder θ_0 is defined as the angle between the xy plane and the axis of the cylinder as shown in Fig. 3. The water surface elevation is set as approximately 0.005–0.010 m below the cylinders in all cases.

The flowchart of the remaining numerical setup process is shown in Fig. 4. The sliding mesh (within the green contour in Fig. 3) is generated first without the cylinder, by *blockMesh*. This step is followed by the generation of the body-fitted mesh for the cylinder using

snappyHexMesh, a mesh generation utility provided in OpenFOAM. The outer mesh is created subsequently by using *blockMesh* again, after which the two meshes are merged by *mergeMeshes*. Note that the dynamic mesh handling class (*sixDoFAMI*) described in Section 2.2 requires the division of the transition and mesh motion zones in the outer mesh, prior to the simulation. These two zones are first marked as different cell zones at the mesh generation stage. After using the utility *setSet* to convert cell zones to face zones, and then to point zones, the grid points can finally be handled by *sixDoFAMI*. Subsequently, before executing the solver, the boundary condition of the sliding interface needs to be specified.

3. Results and discussion

The results of the convergence tests are given first in this chapter, together with the model validation. In Sections 3.2 and 3.3, the results of the cases with different length to diameter ratios and water entry angles are presented and discussed, the focus is on the effects of the above parameters on cylinder's hydrodynamic force and motion. An empirical equation is then proposed to quantify the effects of various parameters on the hydrodynamic force of water entry of the inclined cylinders in Section 3.4.

3.1. Convergence tests and validation

The convergence tests were carried out based on the experimental setup in Wei and Hu (2015). Five combinations of the resolutions of the sliding and outer meshes were chosen. After applying *snappyHexMesh* for generating the body-fitted mesh of the cylinder, the total numbers of cells in the computational domain were 1.43, 2.12, 2.57, 4.27 and 5.34 million, respectively. The cylinder dimensions (the length L and the diameter D) were 200 mm and 50 mm. The cylinder density ρ_s was 900 kg/m^3 and its mass m_s was approximately 0.353 kg. In the convergence test case, the inclined cylinder entered into water with an initial vertical velocity $V_0 = 6.11 \text{ m/s}$ and a water entry angle $\theta_0 = 55.6^\circ$. The cylinder performed free-fall motion under its gravity after the simulation starts.

The snapshots of the numerical water entry of the inclined cylinder at the selected moments in time are shown in Fig. 5, together with the corresponding mesh movement. The origin of time t is defined as the moment when the cylinder starts to interact with the water body. At $t = 1 \text{ ms}$, the cylinder has intruded into the water surface. With the falling cylinder pushes the surrounding water, an air cavity is formed at $t = 25 \text{ ms}$. With the continuous falling and rotation of the cylinder, more cavities are created and then pinches off ($t = 150 \text{ ms}$). The cylinder rotates to the vertical position and tends to float back towards the water surface at $t = 1000 \text{ ms}$ due to its lower density than water. Further,

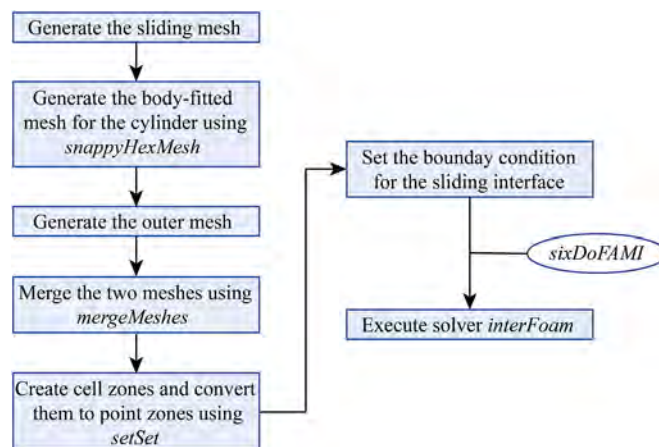


Fig. 4. Flowchart of the numerical setup for the water entry of the inclined cylinder.

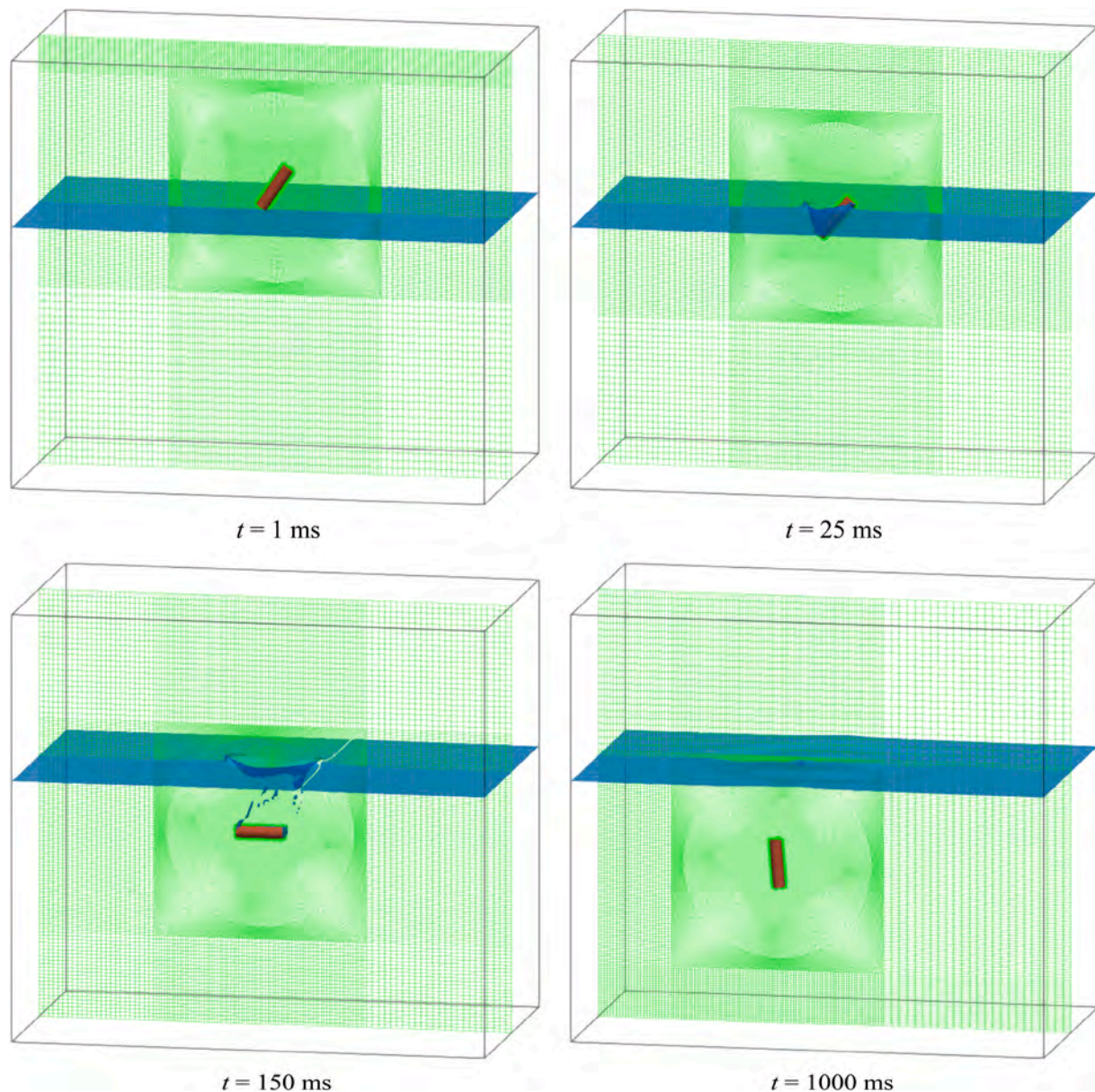


Fig. 5. Snapshots of water surface and the mesh movements in the case with a total cell number of 2.57 million at $t = 1, 25, 150$ and 1000 ms.

regarding the mesh movement in Fig. 5, it can be seen that the newly implemented dynamic sliding mesh handling method can accommodate the large amplitude of the cylinder's displacement. The grid orthogonality can be retained with the moving cylinder such that a good quality of mesh is preserved during the entire simulation.

The comparison of snapshots of the present numerical simulation with the laboratory test conducted by Wei and Hu (2015) is shown in Fig. 6. The numerical simulation generally agrees with the laboratory observation. At $t = 2$ ms, the cylinder intrudes the water surface. During the ongoing process of water entry, flow separation occurs ($t = 13$ ms). At $t = 36$ ms, a cavity above the CoR of the cylinder is formed and continues to grow ($t = 53$ ms). However, during the entire water entry process of the inclined cylinder, the splashes and the thin water films observed in the laboratory test cannot be numerically reproduced. This is because the chosen resolution is not small enough to simulate these phenomena. Nevertheless, the numerical simulation has a good agreement with the laboratory test on the evolution of the cavity shape such as the formation and the growth.

Fig. 7 presents the vertical velocity of the cylinder with different grid

resolutions, along with the results from another numerical study Nguyen et al. (2021). All the present numerical results agree well with the laboratory measurements, even for the coarsest resolution case. Compared with the laboratory results, the present numerical velocity has a maximum deviation of about 0.17 m/s, which is 2.8% of the initial water entry velocity. This demonstrates that the proposed numerical modeling is capable of simulating the water entry of the inclined cylinder. Given that increasing the resolution (higher than 2.57 million cells) does not improve the results significantly, i.e. the results are converged, the mesh with 2.57 million cells was thus chosen for further simulations in this work.

The time history of the relative vertical pressure force F_{pz} and the cylinder's angular velocity is shown in Fig. 8, along with the comparison with those in Wei and Hu (2015) and Nguyen et al. (2021). A good agreement is obtained on the maximum vertical pressure force $F_{pz,m}$ between the present result and that in Nguyen et al. (2021), with a deviation of 5.8% . The second peak in Fig. 8(a) is due to the cavity impact (Sui et al., 2021; Wang and Soares, 2020). Since the chosen resolution is not high enough to capture the cavity evolution accurately, the second

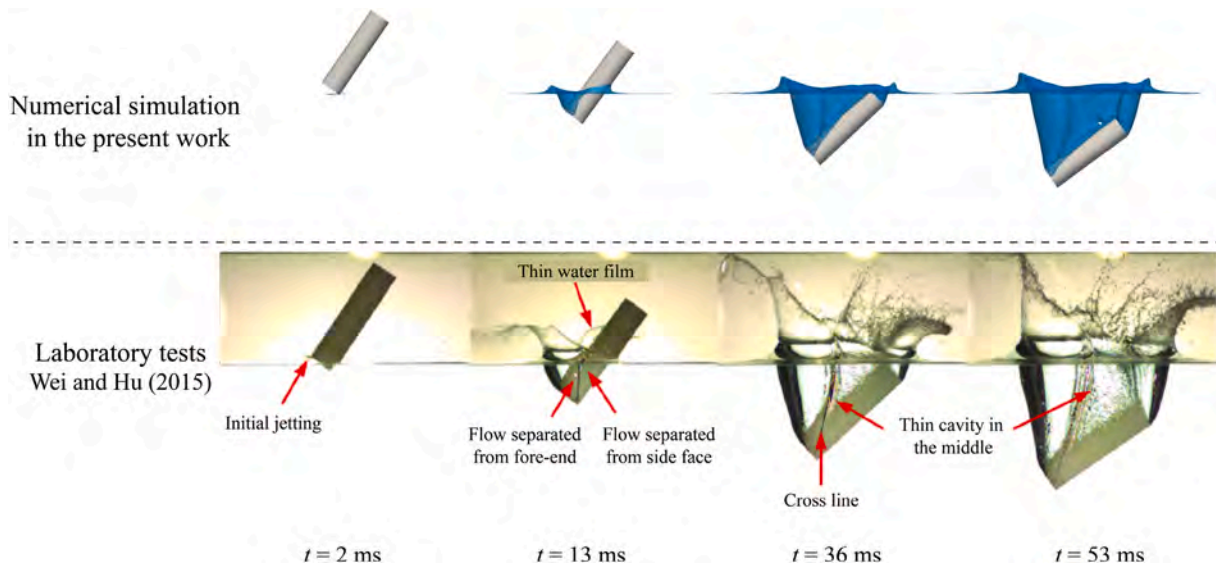


Fig. 6. Snapshot series of the numerical simulation (the case with 2.57 million cells) at $t = 2, 13, 36$ and 53 ms, together with the laboratory observations at the corresponding moments (adapted from Wei and Hu, 2015).

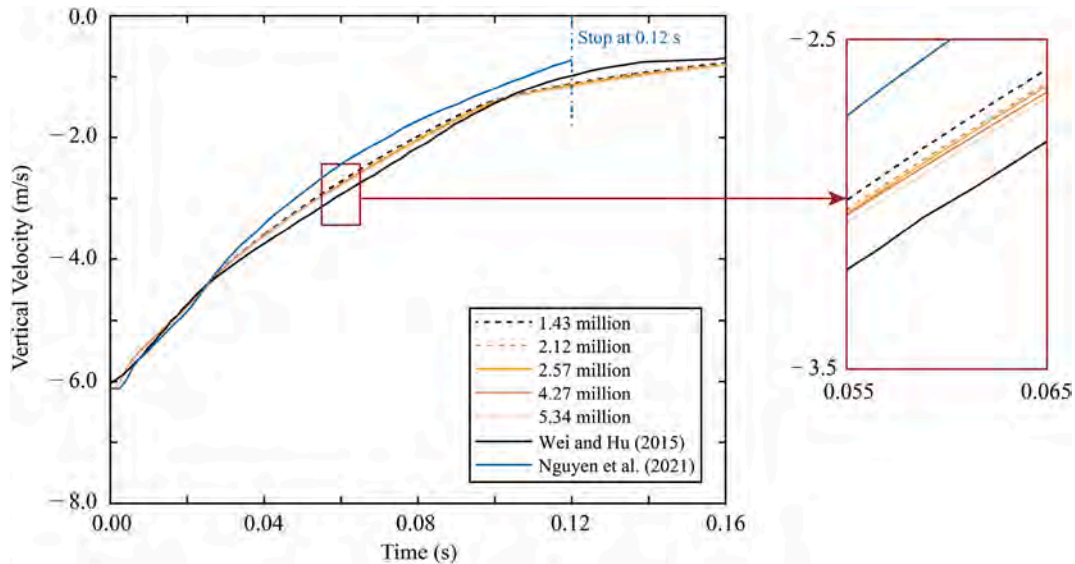


Fig. 7. Time history of the vertical velocity of the falling cylinder in the convergence tests.

peak of the impact load may be underestimated. For the angular velocity, the present numerical result generally agrees with the laboratory measurement, especially in the maximum value. The above comparisons further illustrate that the proposed numerical model can reasonably well reproduce the water entry of the inclined cylinder under the chosen resolution (2.57 million cells).

3.2. Effect of diameter-length ratio

For a given mass of a cylinder, various ratios of diameter to length D/L can result in the different hydrodynamic forces, thus affecting the motion of the cylinder (the velocity and the trajectory). In this section, 7 different D/L were considered. All the cylinders had the same density ($\rho_s = 900 \text{ kg/m}^3$) and impacted into the water at three different water entry angles ($\theta_0 = 30.0, 40.0, 55.6^\circ$). The dimensions of the cylinders together with the parameters of the cases' setup are listed in Table 1. The numerical simulations were conducted on a High Performance Computing cluster. By using 40 cores, each case took approximately 10 h to

complete the simulation of 1.0 s of the water entry process.

Fig. 9 shows the time series of the numerical pressure force components (vertical F_{pz} and horizontal F_{px}) under the conditions of different D/L for each θ_0 . The component F_{pz} always points upwards, while F_{px} can vary in directions during the entire water entry process. The magnitude of F_{pz} is generally larger than that of F_{px} for each θ_0 , i.e. F_{pz} is the dominated hydrodynamic force during the water entry. Compared with F_{pz} , F_{px} tends to become zero with the continuous falling of the cylinder, while F_{pz} tends to stabilise at a certain value. For the maximum vertical pressure force $F_{pz,m}$, it is found that increasing D/L can lead to larger $F_{pz,m}$. This is relevant to the slamming area formed by the cylinder impacts into the water surface. Distributions of the water pressure fields of the selected cases at $\theta_0 = 55.6^\circ$ at the cross-section $y = 0$ when $F_{pz,m}$ occurs are shown in Fig. 10. Except from the $D/L = 0.054$ case where the $F_{pz,m}$ is achieved when a large part of the cylinder is submerged in the water, $F_{pz,m}$ in the remaining cases generally appears when the cylinder's bottom face is nearly wetted. For the $D/L = 0.054$ case, the pressure on the cylinder's side surface is larger than that on its bottom face. In contrast,

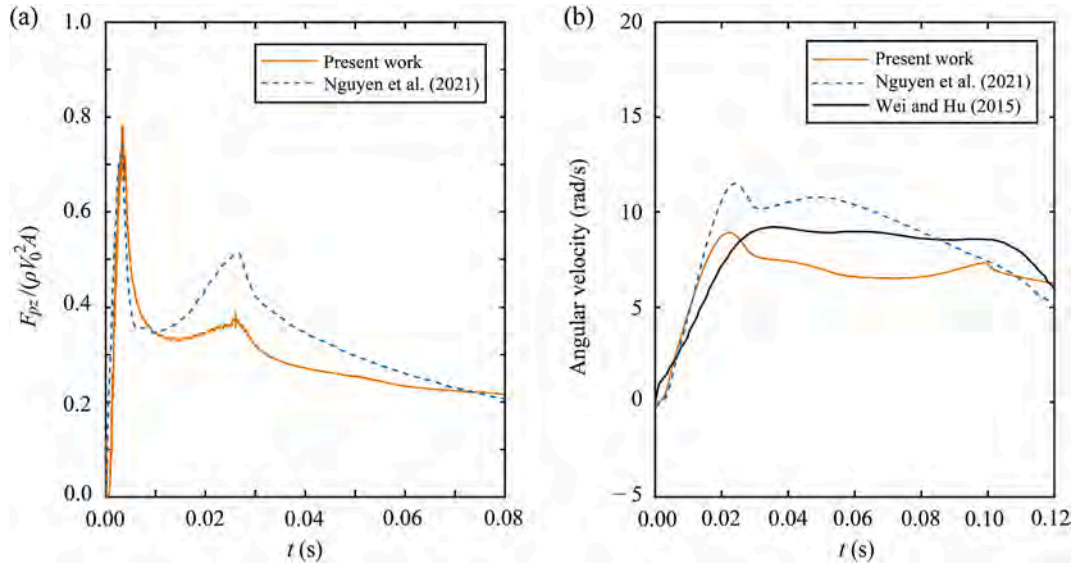


Fig. 8. Comparison of the present results with other work: (a) Relative vertical pressure force versus dimensionless time and (b) time series of angular velocity during the water entry.

Table 1
Parameters in the numerical setup for the water entry of the inclined cylinder.

Diameter D (mm)	Length L (mm)	D/L	Moment of Inertia about y-axis	Water entry velocity	Water entry angle θ_0 ($^\circ$)
			I_y (kg \cdot mm 2)	V_0 (m/s)	
30.00	555.56	0.054	9110	6.11	30.0, 40.0, 55.6
35.00	408.16	0.086	4934	6.11	30.0, 40.0, 55.6
40.00	312.50	0.128	2912	6.11	30.0, 40.0, 55.6
45.00	246.91	0.182	1840	6.11	30.0, 40.0, 55.6
50.00	200.00	0.250	1233	6.11	10.0, 20.0, 30.0, 40.0, 55.6, 78.4
60.00	138.89	0.432	648	6.11	30.0, 40.0, 55.6
70.00	102.04	0.686	415	6.11	30.0, 40.0, 55.6

$F_{pz,m}$ in other D/L cases is mainly contributed by the pressure on the bottom face. Therefore, for cases where the high pressure zone forms on the cylinder's bottom, a higher D/L indicates a larger D (for cylinders with the same mass) and can result in a larger $F_{pz,m}$.

Further, regarding the cases with D/L less than 0.432, two peaks of F_{pz} are observed. This may be due the sudden change in pressure during the evolution of air cavities (Greco et al., 2009; Sun et al., 2021). For the peak F_{pz} values, the first peak in each case is lower than the second one at $\theta_0 = 30.0$ and 40.0° (Fig. 9a) and b). While the first peak is larger at $\theta_0 = 55.6^\circ$, the second peaks reach approximately the same value (28.00 N) as shown in Fig. 9(c).

The velocities of the falling cylinders with different D/L are shown in Fig. 11. The time series of the vertical velocity show a similar trend for each θ_0 . Since the higher D/L causes a larger F_{pz} , the cylinder with a higher D/L moves slower than that with a lower D/L at the beginning. Note that $F_{pz,m}$ corresponds to a lower D/L occurs at a later moment in time, i.e. the cylinder with lower D/L decelerates later. Thus, the deviations among the vertical velocities of cases with different D/L then become smaller. For the horizontal velocity, its maximum magnitude decreases with the growing D/L . When D/L is less than 0.432, the

direction of horizontal velocity generally remains the same (along the negative direction of the x-axis), while the direction may vary when D/L is higher than 0.432 as illustrated in Fig. 11(b) and (c).

Noting that all the inclined cylinders will theoretically become horizontal to reach the final equilibrium, only the time range of the first 0.16 s was selected to compare the rotation angle $\Delta\theta$. The time histories of the rotation angles during water entry of the inclined cylinders among different D/L and θ_0 are shown in Fig. 12. At $t = 0.16$ s, $\Delta\theta$ increases with the increasing D/L in the cases with $\theta_0 = 30.0^\circ$, as shown in Fig. 12(a). By comparison, $\Delta\theta$ at $t = 0.16$ s increases first and then decreases after a specific value, with the growing D/L ratio in the $\theta_0 = 40.0^\circ$ and 55.6° cases. This is because that the cylinder with large D/L has a small I_y , indicating that its ability to resist the rotation is relatively weak. When D/L exceeds a certain value, the decreased L results in a reduced torque and thus a smaller $\Delta\theta$. Further, this certain value may be related to θ_0 . The reason why the $\theta_0 = 30.0^\circ$ cases show the different trending may be due to that D/L does not reach that value.

3.3. Effect of water entry angle

In this section, numerical results of the cases with different θ_0 are presented and the effect of θ_0 on the pressure force is discussed. Since F_{pz} is larger than F_{px} in all cases, F_{pz} is dominant in the cylinder's motion. Therefore, it will be focused on in the remaining sections of this work. Note that there are slight numerical oscillations shown in the time series of F_{pz} (Fig. 9). In order to reduce the influence of the numerical oscillation on $F_{pz,m}$, a moving average filter was applied in MATLAB to filter F_{pz} , in consideration of its simplicity and ease of use. After several tests, a window width of 10 was chosen to reduce the oscillations. The filtered F_{pz} was used for the following data processing in this work. $F_{pz,m}$ versus different D/L at three θ_0 is presented in Fig. 13. It is found that θ_0 affects $F_{pz,m}$ and the effect of θ_0 depends on D/L . For $0.054 \leq D/L \leq 0.686$, larger increases of $F_{pz,m}$ between the two neighbouring D/L occur with $\theta_0 = 55.6^\circ$ than those with other θ_0 . When D/L is greater than 0.128, the cases with $\theta_0 = 40.0^\circ$ have the smallest $F_{pz,m}$.

In order to further investigate the effect of θ_0 on the vertical pressure force on the cylinder, three additional θ_0 were considered, i.e. there are $\theta_0 = 10, 20, 30, 40, 55.6$ and 78.4° in total. These cases were run with $D = 50$ mm, $L = 200$ mm, $\rho_s = 900$ kg/m 3 and $V_0 = 6.11$ m/s. The remaining numerical parameters were the same as those in Section 3.2. Fig. 14 shows $F_{pz,m}$ at each θ_0 . It is observed that $F_{pz,m}$ decreases with the increasing θ_0 first and then increases. There may be a θ_0 resulting in the

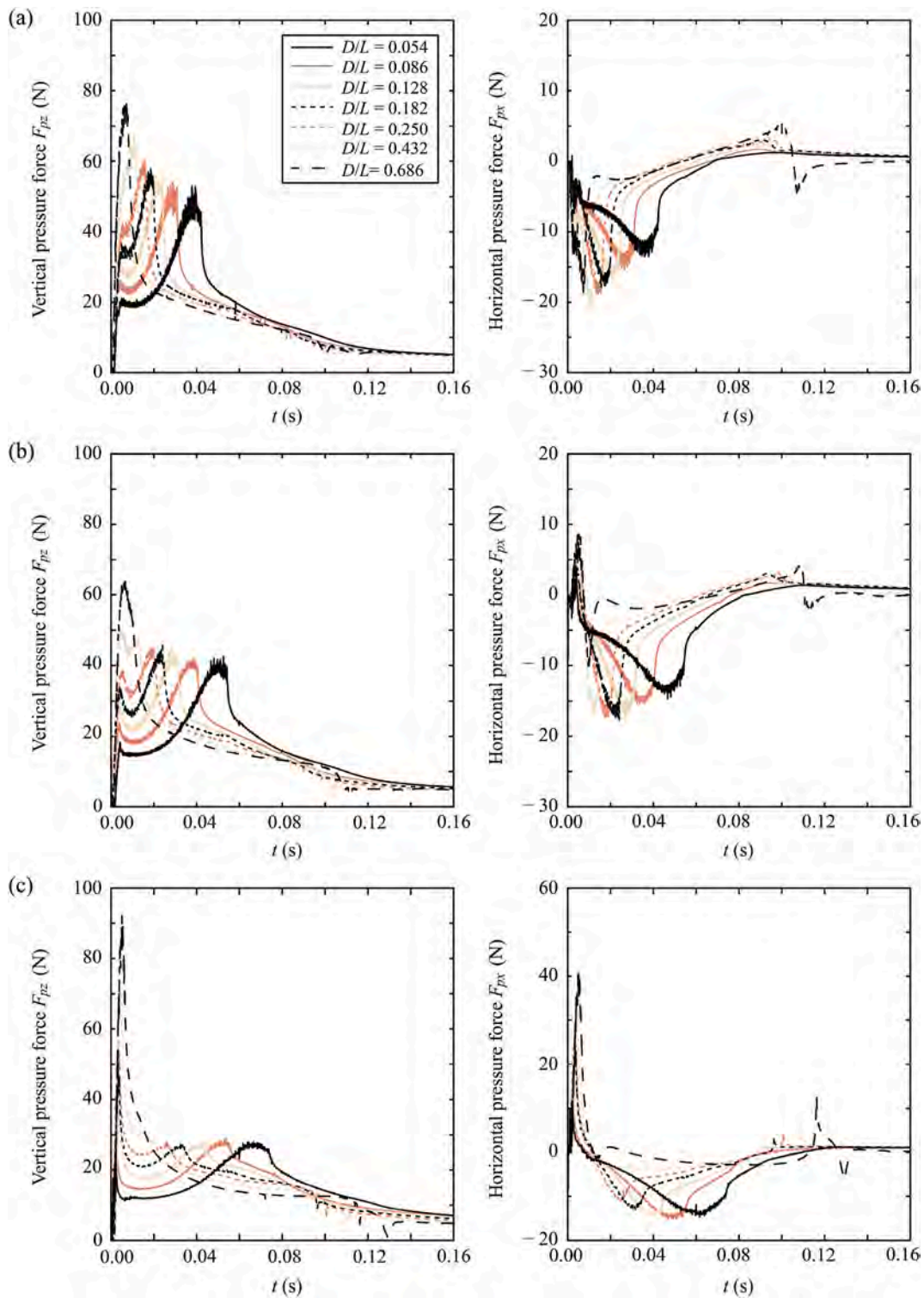


Fig. 9. Time series of the pressure force on cylinders with different D/L ratios at (a) $\theta_0 = 30.0^\circ$, (b) $\theta_0 = 40.0^\circ$ and (c) $\theta_0 = 55.6^\circ$. For legends see (a).

minimum F_{pz} for a certain D/L ratio.

Fig. 15 presents the pressure field distributions of these cases with different θ_0 . When θ_0 is less than 40.0° , the high pressure zone is formed on the side surface of the cylinder. The area of the high pressure zone on the side surface decreases with the growing θ_0 . When θ_0 is larger than 40.0° , the high pressure zone is transferred to the cylinder's bottom surface and the area of the high pressure zone is then enlarged with the increasing θ_0 . By comparing the pressure force in the zones near the side ($\theta_0 = 10.0^\circ$) and bottom ($\theta_0 = 78.4^\circ$) surfaces, it is found that the

cylinder's flat bottom surface can result in large slamming force, although its area is small relative to that of the cylinder's side surface. This is because that the curved geometry of the surface can cause the fluid to flow around the surface such that the water pressure is reduced.

3.4. Various parameters and the slamming force

The pressure force on the cylinder during its water entry process plays a key role in cylinder's structure safety and also its motion state

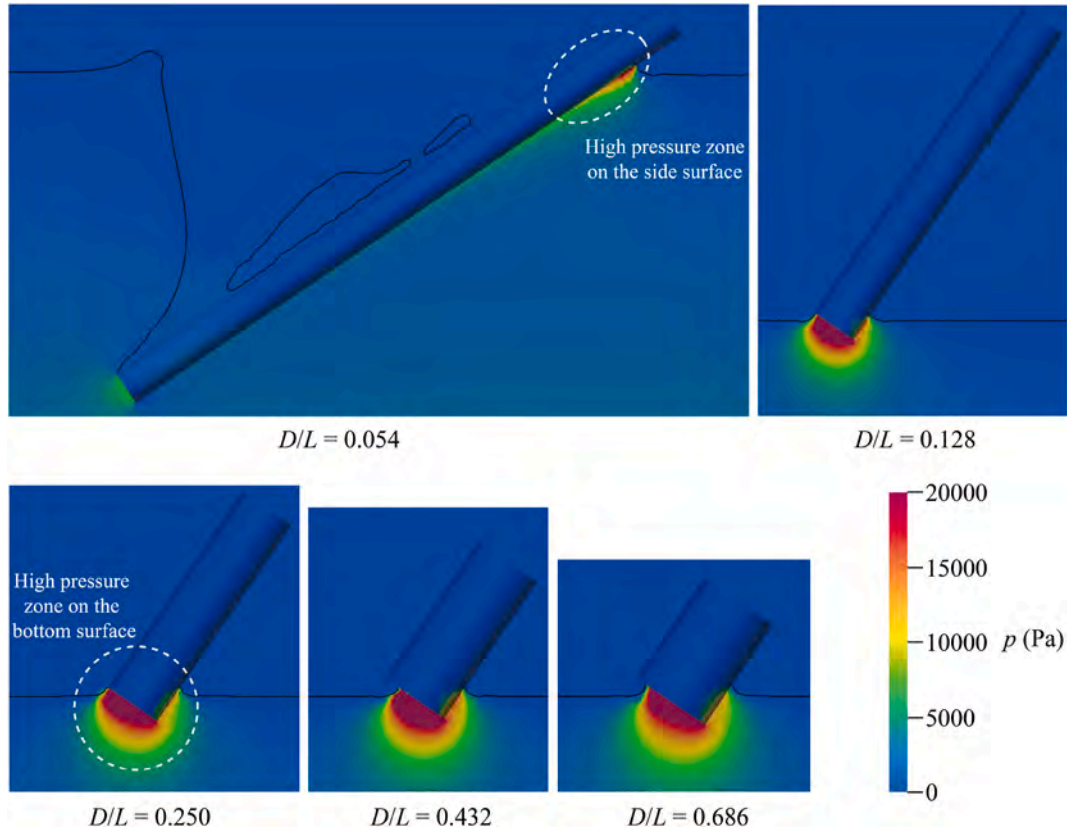


Fig. 10. Snapshots of the pressure field distributions at the xy plane when reaching $F_{pz,m}$ in the cases with different D/L at $\theta_0 = 55.6^\circ$. The time instants of the pressure fields from low to high D/L are 64.00, 4.04, 3.45, 4.07 and 4.85 ms accordingly.

(trajectory and velocity) in real life applications. Based on the results from cases with various D/L and θ_0 , a dimensional analysis was conducted to obtain the correlations of $F_{pz,m}$ with the various parameters (D/L and θ_0). The dimensional analysis method used in this work was Buckingham PI theorem (Buckingham, 1914), which has been widely applied in hydrodynamic problems (e.g. Deng et al., 2016; Heller et al., 2021).

In water entry of the inclined cylinder, there are six independent variables, namely the cylinder density ρ_s , diameter D , length L , water entry velocity V_0 , maximum slamming pressure force $F_{pz,m}$ and the water entry angle θ_0 . The physical units involve the length (m), mass (kg) and time (s) in this work. According to the theorem, there will be three governing dimensionless parameters $\pi_1 = F_{pz,m}/(\rho_s D^2 V_0^2)$, $\pi_2 = D/L$ and $\pi_3 = \theta_0$, after choosing ρ_s , D and V_0 as the fundamental parameters. Therefore, it results in:

$$F_{pz,m} = \rho_s D^2 V_0^2 f\left(\frac{D}{L}, \theta_0\right), \quad (11)$$

where $f\left(\frac{D}{L}, \theta_0\right)$ is the function of D/L and θ_0 . Given that the increment of $F_{pz,m}$ between two different D/L mainly depends on θ_0 , the term about D/L in the above function should be combined with θ_0 . Further, for a given D/L , it tends to result in a large $F_{pz,m}$ when θ_0 approaches to 0 and 90° . The term involving θ_0 in the function should show the symmetry about a certain water entry angle. After testing a selection of functions and trying to retain a concise structure of the function, the specific formats of $f\left(\frac{D}{L}, \theta_0\right)$ in this work is assumed as below:

$$f\left(\frac{D}{L}, \theta_0\right) = c_1 \left(\frac{D}{L}\right)^{c_2 \cos^3\left(\frac{\theta_0}{180^\circ}\pi\right)} \cos^{c_4}\left(\frac{\theta_0 - c_5^\circ}{180^\circ}\pi\right), \quad (12)$$

where the coefficients c_i ($i = 1, 2, 3, 4$ and 5) are determined using

lsqcurvefit function in MATLAB based on the least square method. By taking the numerical results into Eq. (12). The resulted formula of $F_{pz,m}$ is given as:

$$F_{pz,m} = 0.33 \rho_s D^2 V_0^2 \left(\frac{D}{L}\right)^{-0.65 \cos^{1.75}\left(\frac{\theta_0}{180^\circ}\pi\right)} \cos^{-6.48}\left(\frac{\theta_0 - 37.29^\circ}{180^\circ}\pi\right). \quad (13)$$

Here, the coefficient of determination R^2 is introduced to evaluate the fitting error of Eq. (13), which is defined by

$$R^2 = 1 - \frac{\sum (y_{fitted, i} - y_{num, i})^2}{\sum (y_{num, i} - \bar{y}_{num})^2}. \quad (14)$$

By taking the numerical results and fitted values into Eq. (14), $R^2 = 0.99$ is obtained.

Fig. 16 illustrates the fitted $F_{pz,m}$ by Eq. (13) under different D/L and θ_0 , together with the comparison of the results from the fitted and numerical simulations. A high consistency is shown between the fitted and numerical results for various D/L with $\theta_0 = 55.6^\circ$ (Fig. 16a), with the relative differences less than 5.1%. The maximum deviation of $F_{pz,m}$ between the fitted and the numerical results appears at $D/L = 0.054$ and $\theta_0 = 40.0^\circ$, accounting for 16.9% of the numerical $F_{pz,m}$. For the effect of θ_0 on $F_{pz,m}$, as shown in Fig. 16(b), the fitted curve also matches the numerical results. The maximum relative difference between the fitted and numerical $F_{pz,m}$ is -13.6% at $\theta_0 = 40.0^\circ$. In conclusion, for the parameters considered in this work, i.e. $0.054 \leq D/L \leq 0.686$ and $30.0^\circ \leq \theta_0 \leq 55.6^\circ$ together with $\theta_0 = 10.0, 20.0$ and 78.4° at $D/L = 0.250$, all the numerical data are located within the $\pm 16.9\%$ bounds of the corresponding fitted curve. The proposed Eq. (13) is also used to predict $F_{pz,m}$ in cases from other studies. Table 2 shows the comparison between the measured $F_{pz,m}$ in other studies and that obtained by Eq. (13). All the relative errors are within the $\pm 20.0\%$ bounds, which also shows the

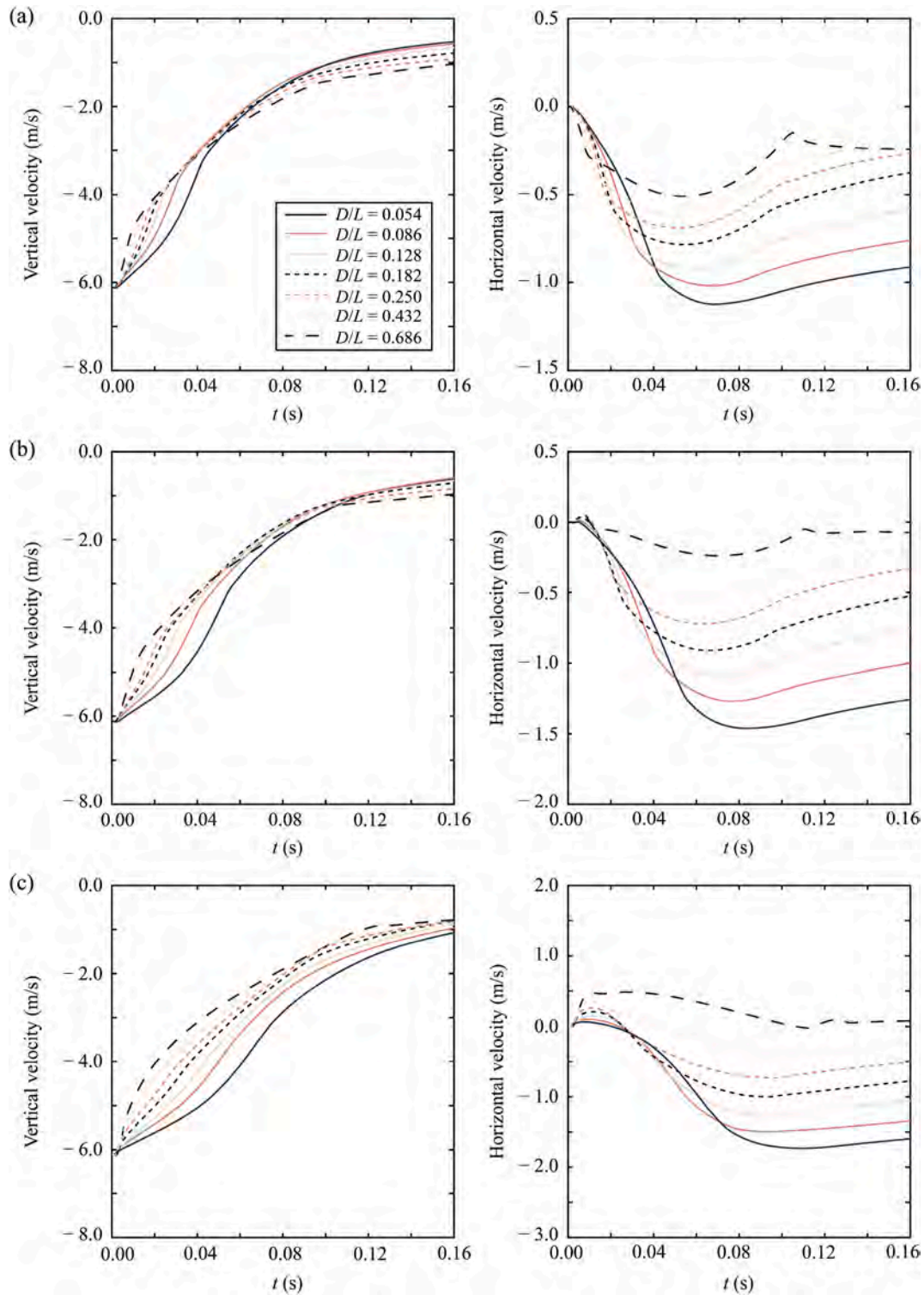


Fig. 11. Velocity components versus time with different D/L at (a) $\theta_0 = 30.0^\circ$, (b) $\theta_0 = 40.0^\circ$ and (c) $\theta_0 = 55.6^\circ$. For legends see (a).

effectiveness in predicting $F_{pz,m}$ during the water entry of inclined cylinders.

4. Conclusions

This article presented a numerical model to simulate the water entry of inclined cylinders. The model was developed based on the multiphase flow solver *interFoam* and the proposed novel dynamic sliding mesh method, within the framework of OpenFOAM. This proposed method

was implemented as a dynamic mesh handling class, which involved the handling of the coupled sliding and outer meshes. A spring-like mesh motion strategy was proposed to perform the mesh morphing within the outer mesh. A six degree-of-freedom motion solver was introduced to resolve the cylinder's motion. This newly implemented dynamic sliding mesh method has the advantages on accommodating the large displacement of an object and maintaining a good mesh quality. Further, it is simple in mesh generation and relatively efficient in computational processes.

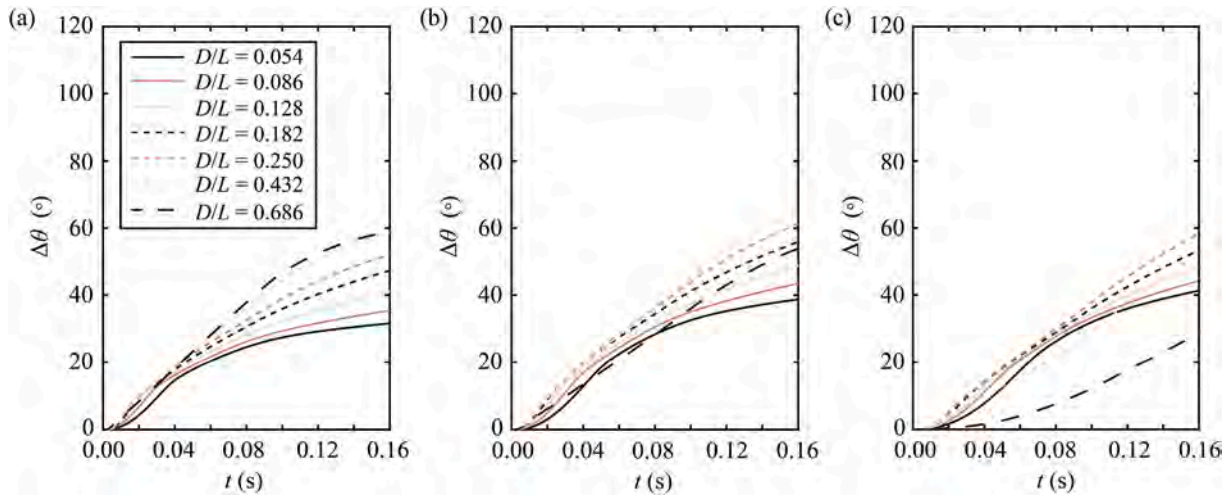


Fig. 12. The changes of the rotation angles after cylinders impact into water with (a) $\theta_0 = 30.0^\circ$, (b) $\theta_0 = 40.0^\circ$ and (c) $\theta_0 = 55.6^\circ$.

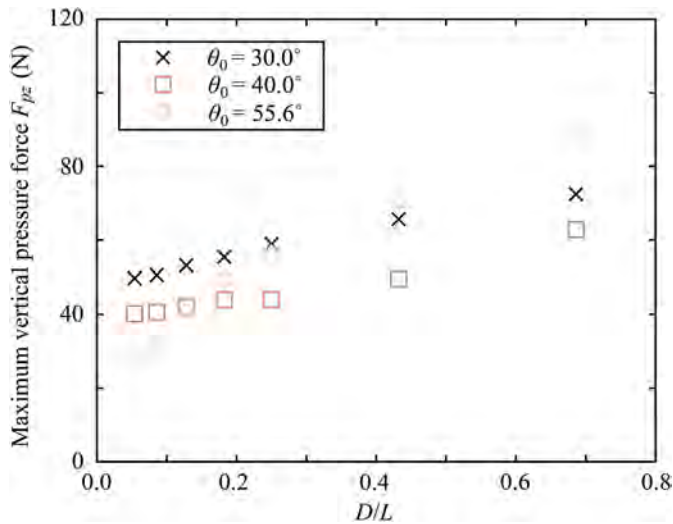


Fig. 13. Maximum vertical pressure force F_{pz} versus diameter to length ratio at three θ_0 .

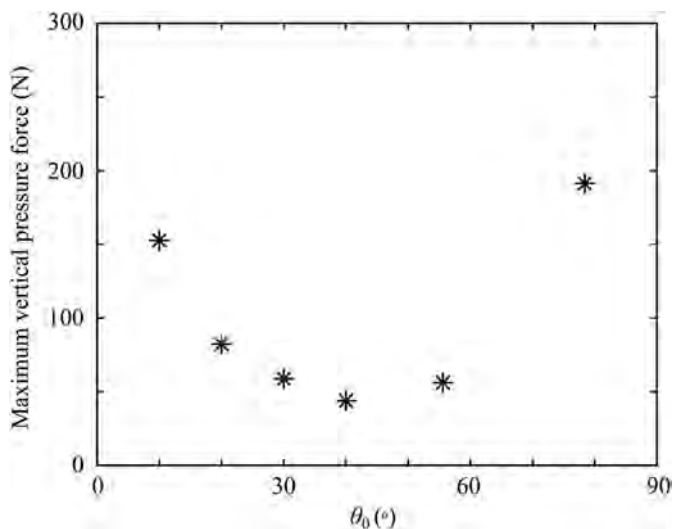


Fig. 14. The maximum vertical pressure force $F_{pz,m}$ under different θ_0 .

After validating with a laboratory experiment and another numerical simulation, this numerical model demonstrates its suitability and accuracy in simulating the fluid-structure interaction in water entry problems. The research's focus was on the investigation of the effects of various parameters on the pressure force on the cylinders with the same mass. These variable parameters involve different diameter to length ratios D/L and water entry angles θ_0 . The velocity and rotation angle of the cylinder with these parameters were also investigated. The main conclusions are drawn as follows: For a given water entry angle, the maximum dominated vertical pressure force $F_{pz,m}$ increases with the growing D/L . For cylinders with the same D/L , $F_{pz,m}$ first becomes smaller and then larger with the increasing θ_0 . Further, a dimensional analysis was conducted based on the Buckingham PI theorem and an empirical equation was proposed, which results in the coefficient of determination of $R^2 = 0.99$ within the range of parameters considered in this work. The numerical results are well captured by the equation, with a maximum relative deviation of 16.9%. Then the equation was applied to predict $F_{pz,m}$ in other studies, resulting in the relative error bound of $\pm 20.0\%$. This proposed empirical equation can provide some guidance on practical applications.

In future work, the characteristics of the flow field such as the evolutions of cavities and vorticities during the water entry of inclined cylinders will be investigated. The proposed empirical equation for $F_{pz,m}$ will be expanded for the water entry of cylinders with a wider range of parameters. The proposed numerical model can also be used for simulations of other fluid-structure interaction problems in coastal and ocean engineering, e.g. the simulation of impulse waves generated by moving masses and ship hull slamming.

Data availability

The data that support the findings of this study are available from the corresponding author upon reasonable request.

CRediT authorship contribution statement

Fan Chen: Conceptualization, Methodology, Data curation, Writing – original draft, preparation, Visualization, Investigation, Software, Validation. **Wenjie Zhong:** Software, Data curation, Visualization, Investigation, Validation. **Decheng Wan:** Supervision, Conceptualization, Methodology, Investigation, Writing – review & editing.

Declaration of competing interest

The authors declare that they have no known competing financial

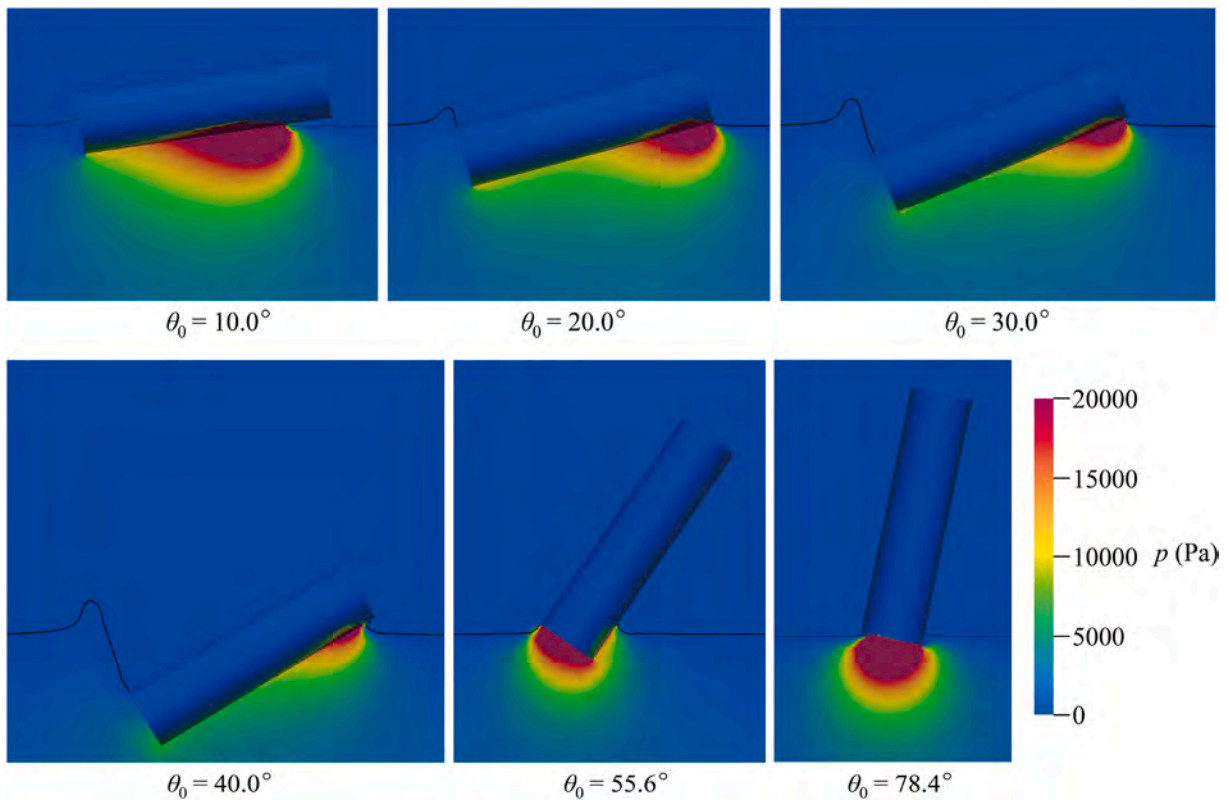


Fig. 15. The pressure fields of the cases with different θ_0 when reaching $F_{pz,m}$. The time instants of the pressure fields from low to high θ_0 are 5.87, 10.96, 15.55, 18.88, 3.45 and 2.23 ms accordingly.

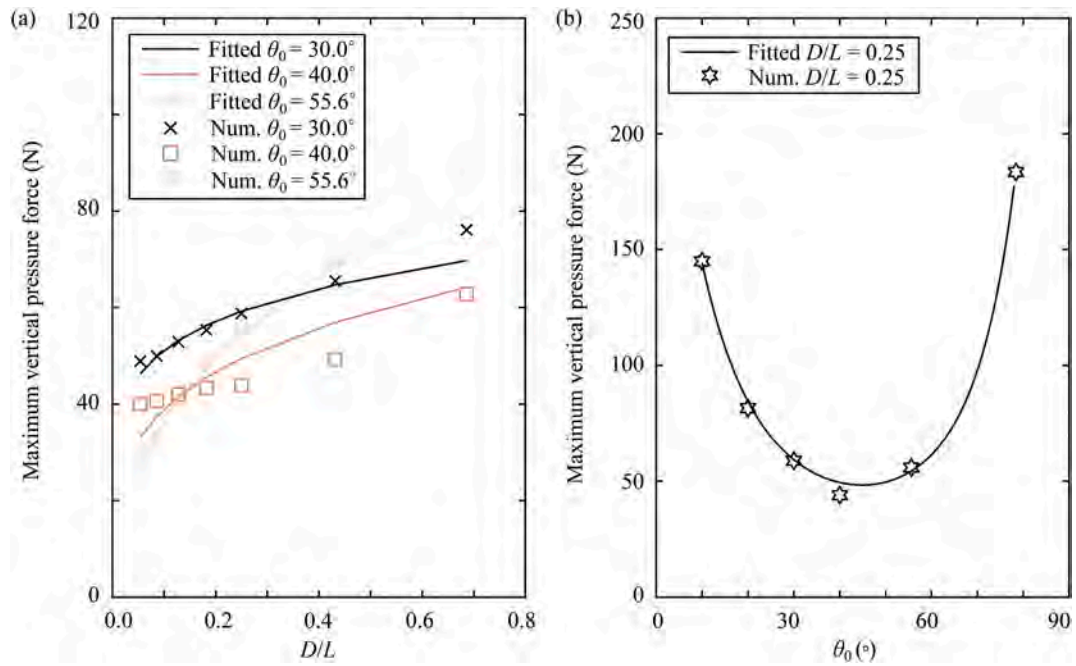


Fig. 16. Comparison of $F_{pz,m}$ between the fitted and numerical (filtered) results under (a) different D/L and (b) various θ_0 at $D/L = 0.25$.

Table 2
Comparison of $F_{pz,m}$ in other studies with that predicted by Eq. (13).

Study	ρ_s (kg/m ³)	θ_0 (°)	D (mm)	D/L	V_0 (m/s)	$F_{pz,m}$ (N)	Predicted by Eq. (13) (N)	Relative error (%)
Liu et al. (2020)	900	78.4	50	0.25	3.05	41.95	45.67	8.88
	900	78.4	50	0.25	6.10	158.39	182.67	15.33
	900	78.4	50	0.25	9.15	342.63	411.02	19.96
	1370	55.6	50	0.25	6.11	71.79	82.33	14.68
Nguyen et al. (2021)	1370	55.6	50	0.25	8.00	173.03	180.28	4.19
	1370	55.6	50	0.25	10.00	388.71	360.56	-7.24
	3000	55.6	50	0.25	6.11	127.35	141.14	10.83
	6000	55.6	50	0.25	6.11	201.01	220.53	9.71

interests or personal relationships that could have appeared to influence the work reported in this paper.

Acknowledgements

This work was supported by the National Natural Science Foundation of China (52101366, 52101324, 51879159, 52131102), and the National Key Research and Development Program of China (2019YFB1704200), to which the authors are most grateful.

References

- Barjasteh, M., Zeraatgar, H., Javaherian, M.J., 2016. An experimental study on water entry of asymmetric wedges. *Appl. Ocean Res.* 58, 292–304.
- Beaudoin, M., Jasak, H., 2008. Development of a generalized grid interface for turbomachinery simulations with OpenFOAM. In: *Open Source CFD International Conference 2008*. Berlin, Germany.
- Buckingham, E., 1914. On physically similar systems; illustrations of the use of dimensional equations. *Phys. Rev.* 4 (4), 345.
- Cooker, M.J., Peregrine, D.H., 1995. Pressure-impulse theory for liquid impact problems. *J. Fluid Mech.* 297, 193–214.
- Deng, Y., Yang, J., Zhao, W., Li, X., Xiao, L., 2016. Freak wave forces on a vertical cylinder. *Coast. Eng.* 114, 9–18.
- Greco, M., Colicchio, G., Faltinsen, O.M., 2009. Bottom slamming for a very large floating structure: uncoupled global and slamming analyses. *J. Fluid Struct.* 25 (2), 406–419.
- Greenhow, M., Lin, W.M., 1983. *Nonlinear-free Surface Effects: Experiments and Theory*. Department of Ocean Engineering, Massachusetts Institute of Technology, Cambridge.
- Heller, V., Attili, T., Chen, F., Gabl, R., Wolters, G., 2021. Large-scale investigation into iceberg-tsunamis generated by various iceberg calving mechanisms. *Coast. Eng.* 163, 103745.
- Hou, Z., Sun, T., Quan, X., Zhang, G., Sun, Z., Zong, Z., 2018. Large eddy simulation and experimental investigation on the cavity dynamics and vortex evolution for oblique water entry of a cylinder. *Appl. Ocean Res.* 81, 76–92.
- Iranmanesh, A., Passandideh-Fard, M., 2017. A three-dimensional numerical approach on water entry of a horizontal circular cylinder using the volume of fluid technique. *Ocean Eng.* 130, 557–566.
- Jasak, H., 2009. Dynamic mesh handling in OpenFOAM. In: *47th American Institute of Aeronautics and Astronautics. AIAA*, Orlando, Florida, USA.
- Liang, H., Zhang, D., Yang, J., Tan, M., Huang, C., Wang, J., Chen, Y., Xu, C., Sun, K., 2016. Hydrodynamic research of a novel floating type pendulum wave energy converter based on simulations and experiments. In: *IEEE OCEANS 2016-Shanghai*, pp. 1–4. Shanghai, China.
- Liu, Y., Xiao, Q., Incecik, A., Peyrard, C., Wan, D., 2017. Establishing a fully coupled CFD analysis tool for floating offshore wind turbines. *Renew. Energy* 112, 280–301.
- Liu, H., Zhou, B., Han, X., Zhang, T., Zhou, B., Gho, W.M., 2020. Numerical simulation of water entry of an inclined cylinder. *Ocean Eng.* 215, 107908.
- Ma, Z.H., Qian, L., Martinez-Ferrer, P.J., Causon, D.M., Mingham, C.G., Bai, W., 2018. An overset mesh based multiphase flow solver for water entry problems. *Comput. Fluids* 172, 689–705.
- Menter, F.R., Kuntz, M., Langtry, R., 2003. Ten years of industrial experience with the SST turbulence model. In: Hanjalic, K., Nagano, Y., Tummers, M. (Eds.), *Turbulence, Heat and Mass Transfer 4*. Begell House, Inc.
- Moradi, H., Rahbar Ranji, A., Haddadpour, H., Moghadas, H., 2021. A hybrid model for simulation of fluid-structure interaction in water entry problems. *Phys. Fluids* 33 (1), 017102.
- Nguyen, V.B., Do, Q.V., Pham, V.S., 2020. An OpenFOAM solver for multiphase and turbulent flow. *Phys. Fluids* 32 (4), 043303.
- Nguyen, V.T., Phan, T.H., Duy, T.N., Park, W.G., 2021. 3D simulation of water entry of an oblique cylinder with six-degree-of-freedom motions using an efficient free surface flow model. *Ocean Eng.* 220, 108409.
- Rodríguez, C.A., Rosa-Santos, P., Taveira-Pinto, F., 2020. Hydrodynamic optimization of the geometry of a sloped-motion wave energy converter. *Ocean Eng.* 199, 107046.
- Seddon, C.M., Moatamedi, M., 2006. Review of water entry with applications to aerospace structures. *Int. J. Impact Eng.* 32 (7), 1045–1067.
- Sui, Y.T., Zhang, A.M., Ming, F.R., Li, S., 2021. Experimental investigation of oblique water entry of high-speed truncated cone projectiles: cavity dynamics and impact load. *J. Fluid Struct.* 104, 103305.
- Sun, H., Faltinsen, O.M., 2006. Water impact of horizontal circular cylinders and cylindrical shells. *Appl. Ocean Res.* 28 (5), 299–311.
- Sun, P., Zhang, A.M., Marrone, S., Ming, F., 2018. An accurate and efficient SPH modeling of the water entry of circular cylinders. *Appl. Ocean Res.* 72, 60–75.
- Sun, T., Shi, C., Zhang, G., Zhou, B., Wang, H., 2021. Cavity dynamics of vertical water entry of a truncated cone-cylinder body with different angles of attack. *Phys. Fluids* 33 (5), 055129.
- Sun, T., Zhou, L., Yin, Z., Zong, Z., 2020. Cavitation bubble dynamics and structural loads of high-speed water entry of a cylinder using fluid-structure interaction method. *Appl. Ocean Res.* 101, 102285.
- von Karman, T., 1929. *The Impact of Seaplane Floats during Landing*. National Advisory Committee on Aeronautics, Washington, DC.
- Wagner, H., 1932. Phenomena associated with impacts and sliding on liquid surfaces. *J. Appl. Math. Mech.* 12 (4), 193–215 (In German).
- Wang, S., Soares, C.G., 2020. Effects of compressibility, three-dimensionality and air cavity on a free-falling wedge cylinder. *Ocean Eng.* 217, 107589.
- Wei, Z., Hu, C., 2014. An experimental study on water entry of horizontal cylinders. *J. Mar. Sci. Technol.* 19 (3), 338–350.
- Wei, Z., Hu, C., 2015. Experimental study on water entry of circular cylinders with inclined angles. *J. Mar. Sci. Technol.* 20 (4), 722–738.
- Wei, Z., Shi, X., 2012. Evolution of three-dimensional cavitation following water entry of an inclined cylinder. *Theor. Appl. Mech. Lett.* 2 (2), 022002.
- Worthington, A.M., Cole, R.S., 1897. Impact with a liquid surface, studied by the aid of instantaneous photography. *Philos. Trans. R. Soc. Lond. - Ser. A Contain. Pap. a Math. or Phys. Character* 189, 137–148.
- Xia, W., Wang, C., Wei, Y., Li, J., Li, Y., Yang, L., 2020. Position detection method and hydrodynamic characteristics of the water entry of a cylinder with multi-degree motion. *Exp. Fluids* 61 (2), 1–22.
- Xiang, G., Wang, S., Soares, C.G., 2020. Study on the motion of a freely falling horizontal cylinder into water using OpenFOAM. *Ocean Eng.* 196, 106811.
- Yan, H., Liu, Y., Kominarczuk, J., Yue, D.K., 2009. Cavity dynamics in water entry at low Froude numbers. *J. Fluid Mech.* 641, 441–461.
- Zhang, H., Zhou, B., Vogel, C., Willden, R., Zang, J., Zhang, L., 2020. Hydrodynamic performance of a floating breakwater as an oscillating-buoy type wave energy converter. *Appl. Energy* 257, 113996.
- Zhu, X., Faltinsen, O.M., Hu, C., 2007. Water entry and exit of a horizontal circular cylinder. *J. Offshore Mech. Arctic Eng.* 129 (4), 253–264.